ELSEVIER

Surface Science 423 (1999) 189–207

surface science

Temperature dependence of kinetic roughening during metal(100) homoepitaxy: transition between 'mounding' and smooth growth

M.C. Bartelt [a,*], J.W. Evans [b]

[a] *Computational Materials Science Department, Sandia National Laboratories, Livermore, CA 94550, USA*
[b] *Department of Mathematics, and Ames Laboratory, Iowa State University, Ames, IA 50011, USA*

Received 18 November 1996; accepted for publication 30 November 1998

Abstract

From simulations of a realistic lattice-gas model for metal(100) homoepitaxy, we analyze the temperature (T) dependence of the film roughness (or interface width), of the effective roughening exponent, of the local step-density, and of the persistence of the Bragg intensity oscillations. By also analyzing the dependence on T of the lateral mass currents of deposited atoms, we reveal a kinetic phase transition from a regime of 'mounding' at higher T, to a regime of 'reentrant' smooth growth at lower T. Application of these results for the cases of Ag, Fe, and Cu homoepitaxy is discussed. Finally, we also describe some features of the dynamics of deposited atoms that could lead to the recovery of rough growth at very low T.

Keywords: Kinetic roughening; Metal(100) homoepitaxy; Mound formation; Step-edge barriers

1. Introduction

The variation with substrate temperature (T) of the morphology and roughness of growing epitaxial films is not only of fundamental interest, but also of importance with regard to the control of film structure and of associated film properties [1]. Two general observations have guided traditional expectations regarding the T-dependence of homoepitaxial growth. First, the equilibrium structure of a homoepitaxial film typically corresponds to a smooth surface, as the substrate temperature is usually below the thermal roughening transition [2]. Consequently, the roughness of the growing film provides a measure of the deviation from equilibrium. Second, analysis of random deposition for a simple-cubic (SC) crystal geometry with on-top adsorption sites reveals very rough 'Poisson growth' when all thermal diffusion processes are inoperative [3]. This result extends to the case where just downward interlayer transport is inoperative, even if intralayer terrace diffusion is significant. These observations have led to the perception that the roughness of a deposited homoepitaxial film of a given thickness should increase monotonically with decreasing temperature. Film structure at higher temperatures would then reflect efficient equilibration or smoothing, and structure at lower temperatures (where thermal diffusion is inhibited) would reflect kinetically limited roughening.

Behavior in real systems can actually be more complicated. In metal(111) homoepitaxy with

* Corresponding author. Fax: +1 925-294-3231; e-mail: mcb@io.ca.sandia.gov.

0039-6028/99/$ – see front matter
PII: S0039-6028(98)00906-6

threefold hollow (3FH) adsorption sites, the activation barrier for terrace diffusion is often low, leading to the formation of large two-dimensional (2D) islands within each layer [4–8]. Also, there is usually a large Ehrlich–Schwoebel or step-edge activation barrier [9,10] (in addition to the terrace diffusion barrier) that inhibits downward transport at island edges. As a result, one observes rough Poisson-like growth for a broad range of T where islands are large, but downward transport is strongly inhibited. (Note that the above observations for SC crystals apply here since crystal or adsorption site geometry has no significant influence for large 2D islands.) However, for Pt/Pt(111), 'reentrant' smooth growth was observed for low T [4,5]. This unexpected behavior is apparently a consequence of a transition from compact to irregular or fractal 2D islands with lowering T, which in turn leads to enhanced downward transport, possibly due to lower step-edge barriers at kink sites at the edges of irregular islands [11].

Perhaps more surprisingly, similar 'anomalous' behavior occurs for metal(100) homoepitaxy with fourfold hollow (4FH) adsorption sites [for metals where the (100) surface does not reconstruct]. These systems are simpler than those above in that no dramatic transition occurs in the shape of the 2D islands with decreasing T [12]. None the less, unexpected smooth quasi-layer-by-layer film growth was also observed in these systems at low T where terrace diffusion is inoperative [13–15]. This behavior was explained in part by recognizing the smoothing influence of adsorption at 4FH adsorption sites (relative to on-top sites), which requires four atoms in the layer beneath (compared with just one) [16–20]. However, the other key ingredient in producing smooth growth at low T was determined to be the propensity of atoms deposited on top of isolated atoms, at step edges, or on other microprotrusions to funnel downward to lower 4FH adsorption sites [16–20]. For higher T, where near-square islands form in each layer, smooth growth is partly impeded by the presence of a 'small' step-edge barrier. Recent analysis revealed that the film roughness first increases as T decreases from 'high' values, since the step-edge barrier becomes more difficult to surmount, but then reentrant smooth growth occurs for lower T [21–26]. The latter is due to smaller islands, a higher step-density, and thus enhanced downward funneling. Furthermore, the downward funneling process was shown to play a crucial role in determining film morphology even at higher T. We elaborate on these issues below.

In this paper, we provide a comprehensive characterization of the temperature dependence of film growth in a model for metal(100) homoepitaxy, as well as an analysis of the underlying atomistic dynamics that controls this behavior. Specifically, for a fixed film thickness, we examine the dependence on T of the roughness (or interface width), of the effective roughening exponent, of the local step-density, and of the oscillations in the kinematic Bragg intensity at the anti-phase condition. Furthermore, by analyzing the dependence on T of the lateral mass currents of deposited atoms, we show that there is a 'kinetic phase transition' from a regime of unstable growth or 'mounding' for higher T, to a regime of smooth growth at lower T. We also emphasize that behavior of actual systems at low T, around and below the transition, can be controlled by system-specific features of the atomistic dynamics, which are not accounted for in generic modeling. In fact, a quite distinct rough growth mode could emerge at very low T (cf. Refs. [27,28]).

2. Model details and parameters for metal(100) homoepitaxy

We now provide a brief description of our model for metal(100) homoepitaxial growth that incorporates irreversible 2D island formation in each layer (no lateral bond-scission) [21]. The model includes the appropriate 4FH adsorption site geometry and island structure for fcc(100) or bcc(100) metals. Specifically, the 4FH adsorption sites form a square grid in each layer, and the islands formed have near-square shapes with close-packed $\langle 110 \rangle$ or $\langle \bar{1}10 \rangle$ edges aligned along the [100] and [010] principal lattice directions. The schematic of our model in Fig. 1 indicates the following key steps:

1. Atoms are deposited randomly at rate F, mea-

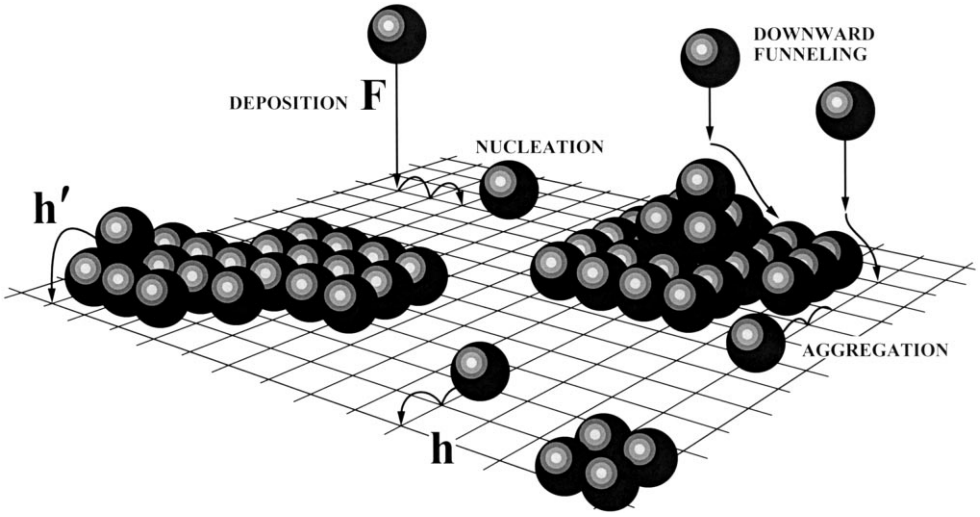

Fig. 1. Schematic of our model for metal(100) homoepitaxial growth without bond-scission.

sured in monolayers (ML) per unit time. Those atoms impinging at 4FH sites adsorb there, whereas those impinging on top of isolated atoms (or dimers or trimers), at step edges, or on other microprotrusions funnel down to lower 4FH sites. A convenient discrete description of deposition dynamics is adopted, which captures these features (see Appendix A).

2. Isolated adatoms hop to adjacent empty 4FH sites in each layer at rate of $h=\nu\exp[-E_d/(k_BT)]$ per unit time (per direction). Such adatoms also hop across descending step edges at a reduced rate $h'=\exp[-E_{se}/(k_BT)]h$, and thereafter funnel down to lower 4FH sites where they are captured. (In fact, there is a finite probability that such adatoms can diffuse back up larger {111} facets, and recross the step edge. However, if diffusion on {111} facets is rapid, then this process is less likely.) Here, E_d is the activation barrier to terrace diffusion, E_{se} is the additional step-edge barrier, and a common attempt frequency, ν, is assumed.
3. When two diffusing adatoms meet, they irreversibly nucleate a new island. A diffusing adatom reaching the edge of an existing island is irreversibly incorporated into that island.
4. During growth, individual islands maintain near-square shapes, with at most one incomplete edge, by the instantaneous incorporation of additional atoms at the kink site. This feature mimics the rapid diffusion of adatoms along close-packed island edges in these systems. A pair of islands does not restructure subsequent to 'collision' resulting from growth, but continues to grow as two overlapping squares.

Next, we review some key quantities of interest, and their expected behavior for this model of film growth. In the submonolayer regime, the mean density of 2D islands, N_{av}, effectively saturates by a rather low value of coverage, θ, for a typical large h/F, and decreases at a much higher θ due to coalescence. At a fixed pre-coalescence θ, one finds the classic scaling behavior for irreversible island formation, $N_{av}\sim(h/F)^{-1/3}$, so N_{av} increases with decreasing T or increasing F. The mean island separation, L_{av}, is trivially related to N_{av}, and satisfies $L_{av}=(N_{av})^{-1/2}\sim(h/F)^{1/6}$ (see Refs. [29–31]). In the multilayer regime, the layer coverage distribution, θ_j, for layers $j\geq 0$, is of primary interest, where $j=0$ denotes the substrate (so $\theta_0=1$). Then, $P_{j\geq 0}=\theta_j-\theta_{j+1}$ gives the fraction of 'exposed' atoms in layer j, and $\Sigma_{j\geq 0}P_j=1$. (Even for a perfectly flat surface of height j, with $P_j=1$ and $P_{k<j}=0$, the atoms in layer $j-1$ are still partly visible through the centers of the 4FH sites, but here, we treat these as 'completely' hidden.) This

distribution determines the interface width, W (in units of the interlayer spacing), via [32]

$$W^2 = \sum_{j\geq 0} (j-j_{av})^2 P_j, \text{ where } j_{av} = \sum_{j>0} \theta_j = \theta. \quad (1)$$

W quantifies the film roughness, and its increase during growth can be typically fitted by the form $W \sim \theta^{\beta}$, where β is the (effective) exponent describing kinetic roughening [32] (although the emergence of this behavior is delayed for quasi-layer-by-layer growth where W displays transient oscillations). Film smoothness during growth is also characterized qualitatively by the persistence of oscillations in the (normalized) kinematic Bragg intensity at the anti-phase condition [21,25,26],

$$I_{BR} = \sum_{j\geq 0} (-1)^j P_j \approx 4\cos^2[\pi\theta - \kappa\pi^3\theta^3 + \ldots] \times \exp[-\pi^2 W^2 + \ldots], \quad (2)$$

where $\kappa = \Sigma_{j\geq 0}(j-j_{av})^3 P_j / W^3$ measures the skewness of the film height distribution. Below, we describe how 'mounds' form during growth in the presence of a step-edge barrier. These generally coarsen during growth with lateral dimension satisfying, $L_m \sim \theta^n$ [32]. If a mound slope is selected, then $n=\beta$. We also consider the 'total' density of ascending plus descending steps (weighted by step height) in the [100] principal lattice direction, which provides some assessment of the 'local slope' of the surface in that direction.

3. Simulation results: temperature dependence of film growth

Below, we consider separately cases of small and large step-edge barriers, E_{se} (relative to the terrace diffusion barrier, E_d), and thus naturally introduce the ratio $\Gamma = E_{se}/E_d$. It is instructive to note that for fixed Γ (and fixed F/ν), the multilayer growth behavior of our model depends only on the ratio E_d/T (or E_{se}/T). Simulation results presented below were obtained on lattices of at least 10^7 sites with periodic boundary conditions.

3.1. Growth behavior for small step-edge barrier

First, we examine the case of small $\Gamma \approx 0.1$, which characterizes Ag/Ag(100) and Fe/Fe(100) homoepitaxy [12]. Specifically, simulation parameters are chosen as $E_d = 325$ meV, $E_{se} = 25$ meV (so $\Gamma \approx 0.077$), $\nu = 10^{12}\,s^{-1}$, and $F = 0.06$ ML s^{-1}, which reasonably describe Ag/Ag(100) homoepitaxy [33–35]. This low step-edge barrier results in smooth growth for a broad range of T, at least in the sense of persistent Bragg oscillations. None the less, kinetic roughening does typically occur with $\beta > 0$. Fairly smooth growth occurs at high $T \approx 300$ K (where $h/F \approx 10^9$), but both W (at, say, 30 ML) and the effective β (measured between 20 and 30 ML) initially increase with decreasing T (or h/F). This trend occurs since the step-edge barrier becomes more difficult to surmount with decreasing T. However, for a much lower T (below about 200 K), the greater influence of downward funneling due to higher step-densities causes a reduction in W and β (see Fig. 2a and b). This non-monotonic behavior, or 'reentrant' smooth growth, has been noted previously [21,22]. Fig. 2c shows the dependence on T of the total step-density (see Section 2) at 30 ML. This density increases monotonically with decreasing T. Finally, examples of oscillatory decay of the Bragg intensity at the anti-phase condition are shown in Fig. 2d, the enhanced oscillations for low T reflecting reentrant smooth growth. Film snapshots obtained in the simulations for various T are shown in Fig. 3.

3.2. Growth behavior for large step-edge barrier

It is also instructive to consider the opposite regime of 'high' Γ. A maximum possible value of $\beta \approx 1/2$ is achieved if both the step-edge barrier is effectively insurmountable at the given T (and the refore also at lower T) and if the 2D islands within each layer are sufficiently large that downward funneling is insignificant. Behavior in the extreme case with $\Gamma = \infty$ is shown in Fig. 4. The results in Fig. 4a and b show a monotonic increase in the roughness with increasing h/F (or T), as is expected since downward funneling diminishes with increasing 2D island size [21]. Again, the step-density increases monotonically with decreasing h/F (or T). See Fig. 4c. Now, the persistence of the Bragg intensity oscillations decreases monotonically with increasing h/F or T (Fig. 4d). However, it should be noted that even for

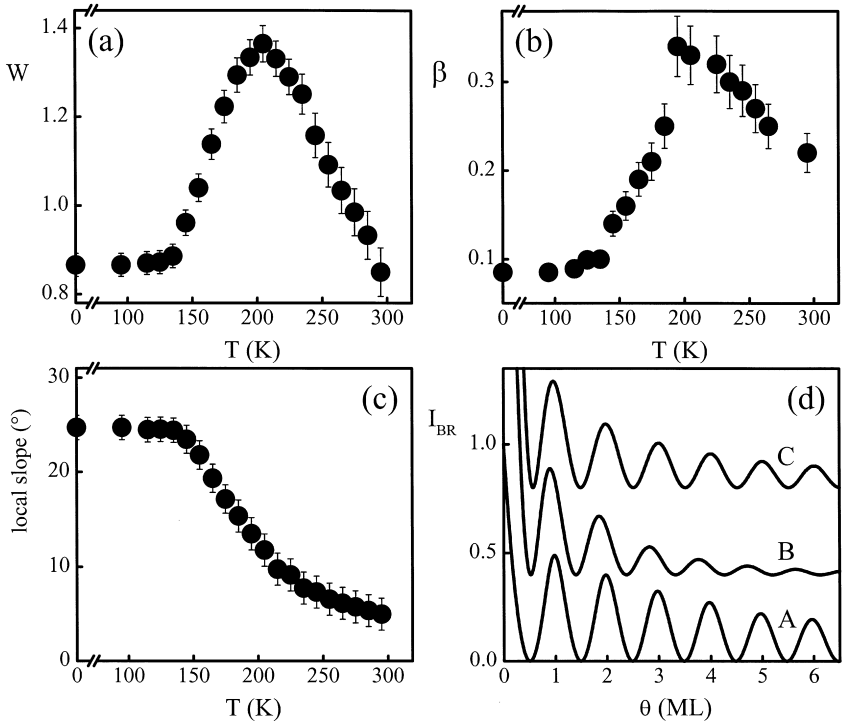

Fig. 2. Temperature dependence of film growth in metal(100) homoepitaxy for small Ehrlich–Schwoebel barrier with $\Gamma = E_{se}/E_d \approx 0.1$. Simulation parameters are chosen to roughly match Ag/Ag(100): $E_d = 325$ meV, $E_{se} = 25$ meV, $\nu = 10^{12}\ s^{-1}$, and $F = 0.06$ ML s^{-1} [33–35]. Results for: (a) W at 30 ML; (b) the effective β determined in the range 20–30 ML (which matches the experimental values [33–35] at both 200 K and 300 K); (c) the local slope determined from the local step-density at 30 ML; (d) anti-phase Bragg intensity oscillations; data were scaled so that the maximum at ~ 1 ML has the same value for all T: A($\times 1$)-300 K; B($\times 4.4$)-200 K; C($\times 9.2$)-100 K. Curves B and C were shifted up for clarity.

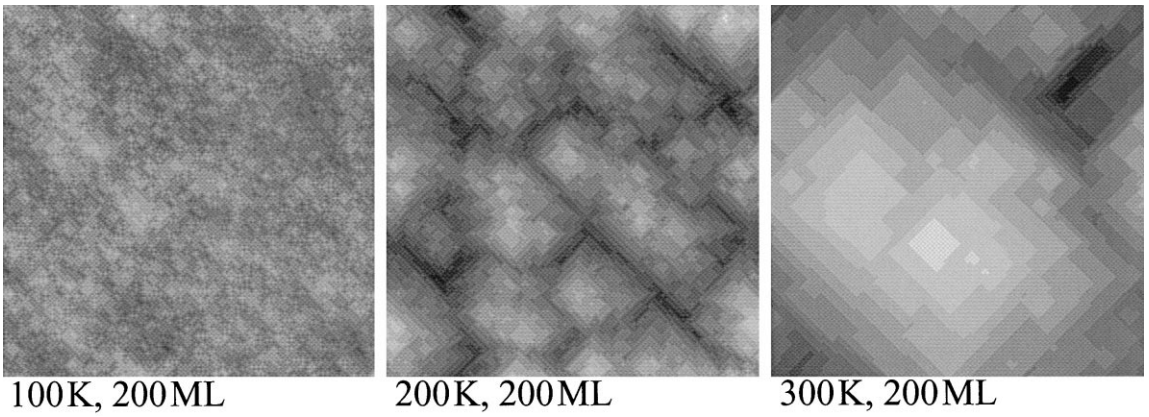

Fig. 3. Snapshots of a $170a/\sqrt{2} \times 170a/\sqrt{2}$ region of 200 ML films obtained in simulations at $T = 100$, 200, and 300 K, as indicated, using $E_d = 325$ meV, $E_{se} = 25$ meV (so $\Gamma \approx 0.08$), $\nu = 10^{12}\ s^{-1}$, and $F = 0.06$ ML s^{-1}. Darker regions have a lower height.

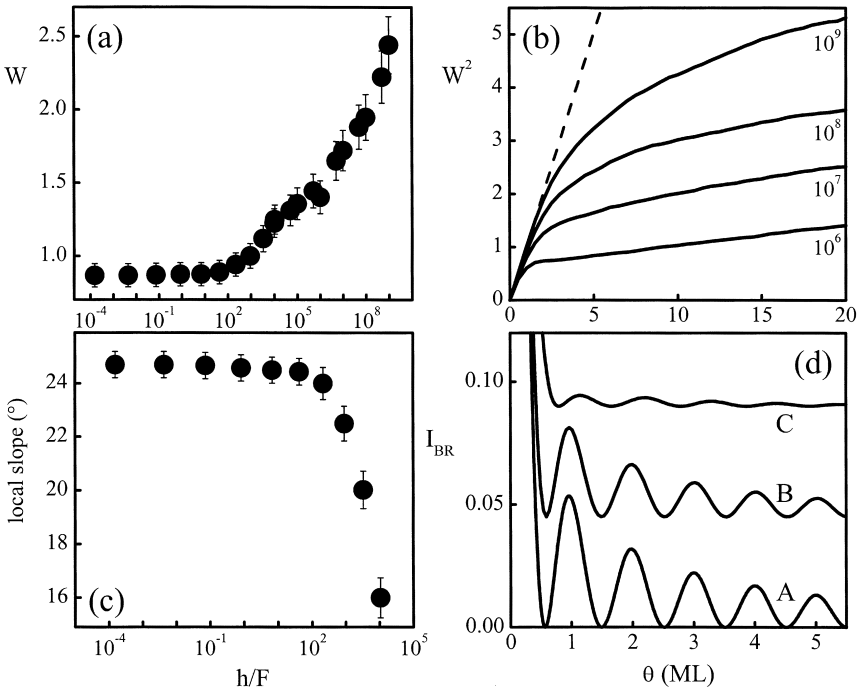

Fig. 4. Dependence on h/F of film growth in metal(100) homoepitaxy for infinite Ehrlich–Schwoebel barrier, so $\Gamma = E_{se}/E_d = \infty$. Simulation results for: (a) W at 30 ML; (b) W^2 versus θ, for $h/F = 10^6$–10^9 as indicated (the dashed line is $W^2 = \theta$); (c) the local slope determined from the local step-density at 30 ML; (d) anti-phase Bragg intensity oscillations (A: $h/F \approx 0$, B: $h/F \approx 10^2$, C: $h/F \approx 10^4$). Curves B and C were shifted up for clarity.

$h/F \approx 10^9$ where islands are sizeable, downward funneling is significant and the effective β (even around 10–20 ML) is far below 1/2. [For any fixed range of film thickness, the effective value of β must approach 1/2 with increasing h/F. Deviations in β from 1/2 will occur at large film thicknesses, when sufficiently steep mounds develop (with mound height comparable to base dimension), and growth reflects the non-SC-geometry. The cross-over thickness to this regime increases with increasing h/F (see Fig. 4c).] The simulation snapshots in Fig. 5 show typical multilayer configurations for a few different T.

3.3. Application to specific systems

3.3.1. Ag/Ag(100)

As noted above, the behavior shown in Fig. 2 for a low step-edge barrier corresponds roughly to Ag/Ag(100) homoepitaxial growth [33–35]. These simulations with $F \approx 0.06$ ML s^{-1} predict that roughening occurs with $\beta \approx 0.2$ at 300 K, but with a substantially higher maximum β of around 0.3 at 200 K (see Fig. 2b). These results (and results, not shown, for the slightly higher experimental $F \approx 0.2$ ML s^{-1}) are in excellent agreement with the observations from experimental surface-sensitive X-ray scattering studies by Elliott et al. [36–38]. We also predict reentrant low values of β below 0.3 for T lower than 200 K. Our simulations show that the 'local slope' in the [100] direction, estimated from the total step-density, increases strongly and monotonically with decreasing T, from about 6° at 300 K. It should be noted that an independent X-ray scattering study by Alvarez et al. [39] suggested that β decreased monotonically with decreasing T from 400 to 150 K in this system. This result appears inconsistent with those of Elliott et al. and with our simulations. However, the analysis of β in [39] was indirect (using a simple heuristic rate-equation model for roughening), it considered data for a narrow range of θ,

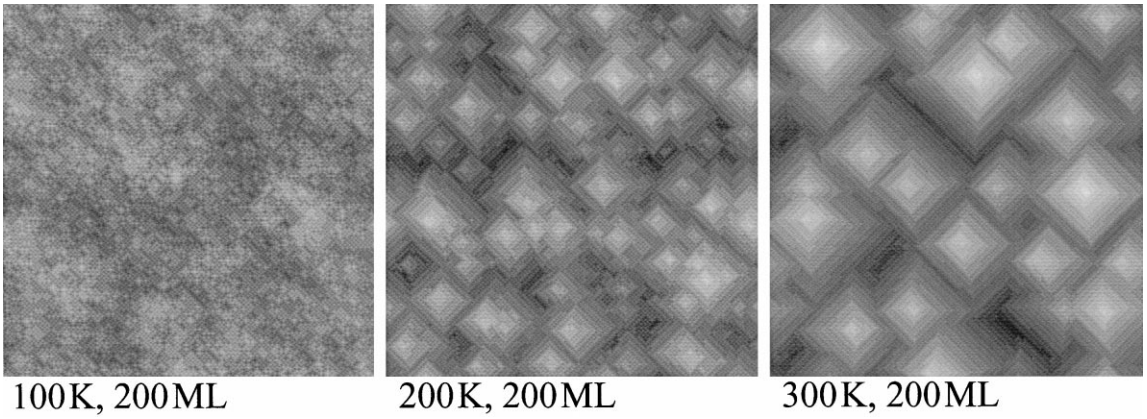

Fig. 5. Snapshots of a $170a/\sqrt{2} \times 170a/\sqrt{2}$ region of 200 ML films obtained in simulations for $h/F \approx 0$, 10^5, and 10^8 (corresponding to $T = 100$, 200, and 300 K, respectively, as indicated, if $E_d = 325$ meV, $\nu = 10^{12}\ s^{-1}$, and $F = 0.06$ ML s^{-1}), and $E_{se} = \infty$. Darker regions have a lower height.

and it corresponded to a much lower value of F than [36–38]. Their more direct analysis of coarsening of the mean lateral mound dimension, $L_m \sim \theta^n$, during growth (for $\theta \leq 6$–8 ML) indicated that n increases from about 0.15 to 0.27 for T decreasing from 300 to 200 K. This is reasonably consistent with the measurements of Elliott et al. and the predictions of our model, if one assumes slope selection of the mounds so that $\beta = n$.

3.3.2. Fe/Fe(100)

From STM studies of Fe/Fe(100) growth [40,41], it was estimated that $E_d \approx 450$ meV with $\nu \approx 10^{11}\ s^{-1}$, and that $E_{se} = 30$–40 meV for our model (so $\Gamma \approx 0.08$) [21–25], and $E_{se} =$ 55–65 meV for a model with diffusion of atoms along close-packed island edges controlled by a barrier of 100–125 meV [42,43]. Thus, the low value of Γ is rather similar to that for Ag/Ag(100). As a result, from the opening discussion in this section, our model predictions for the T-dependence of roughening for Fe/Fe(100) would be similar to those for Ag/Ag(100), for the same h/F. More specifically, behavior observed for Fe/Fe(100) at a given T^* would roughly correspond to that observed for Ag/Ag(100) at a lower $T = [E_d(\mathrm{Ag})/E_d(\mathrm{Fe})]T^* \approx 0.8T^*$. Our simulations reproduce the observed roughening, as well as revealing a 'local slope' obtained from the total step-density of 14° at 295 K for $F \approx 0.01$ ML s^{-1} [22,25,26], consistent with experimental observations [40,41]. (In contrast, such a steep slope is only achieved for Ag/Ag(100) well below 295 K.) Similar success in describing growth of Fe/Fe(100) was obtained in models with finite diffusion of adatoms at island edges [42,43].

3.3.3. Cu/Cu(100)

The pioneering study of kinetic roughening during metal(100) homoepitaxy was actually performed for the Cu/Cu(100) system by Ernst et al. [44,45]. This study not only revealed mound formation with selected slopes, but also assessed the T-dependence of growth. A subsequent study [46] supported these findings. Specific observations of key relevance here were smoother growth at 160 K (where $\beta \approx 0.3$) than at 200 K (where $\beta \approx 0.5$), and a decrease in mound slopes from $\sim 25°$ at 160 K to $\sim 16°$ at 200 K (for $F \approx 0.01$ ML s^{-1}). Certainly, these general trends seem consistent with the predictions of our model in the regime of lower T or h/F. A simplistic interpretation of the observed $\beta \approx 1/2$ at 200 K is that the step-edge barrier is effectively insurmountable at this (and lower) temperatures, assuming that the 2D islands are fairly large. However, choosing $E_d \approx 0.38$ eV and $\nu \approx 10^{11}\ s^{-1}$ to match the measured submonolayer L_{av}-behavior [25,26,47], and setting $\Gamma = \infty$, our model produces far smaller β-values than those

observed, due to significant downward funneling from island edges [25,26].

This discrepancy is likely due to limitations of our model. The structure of the growing Cu/Cu(100) film perhaps reflects thermodynamic factors to a greater extent than for Ag/Ag(100) or Fe/Fe(100). Indeed, the temperature for the transition to reversible island formation during deposition is much lower for Cu ($\sim$230 K) than for Ag ($\sim$320 K) or Fe ($\sim$500 K) [12,25,26], and the rates of post-deposition coarsening, and island restructuring and diffusion are higher for Cu [48–50]. Thus, Cu islands could significantly restructure subsequent to collision (a feature neglected in our model), and perhaps diffusion of adatoms up steep {111} facets and across step edges is more significant. Thermodynamic effects for Cu/Cu(100) are likely reflected in the observed staircase-like T-dependence of the selected slope during growth [46], and in the feature that 'vacancy mounds' formed during ion bombardment of Cu(100) select similar slopes to growth mounds for the same T [51]. A study of Cu/Cu(100) homoepitaxy at 300 K [52] revealed smoother growth ($\beta \approx 0.45$) and a smaller selected slope (2.5°) than at 200 K, and was in fact described in terms of thermodynamic driving forces (e.g. coarsening due to capillarity, and a downhill current driven by step-edge line tension). However, our model with irreversible island formation (where the downhill current has a different origin) produces to some extent the observed trends, so it is difficult to ascribe the observed behavior unambiguously to reversibility.

4. Lateral mass currents controlling film growth

Villain [53] provided the following explanation for the occurrence of 'unstable' epitaxial growth on perfect 'singular' surfaces or substrates in the presence of a step-edge barrier. Such a barrier leads to biased reflection of diffusing adatoms from descending steps and incorporation at ascending steps. This produces a destabilizing lateral mass current, or 'Schwoebel' current, $\underline{J}^{up}$, in the uphill direction, and results in the formation of mounds that may coarsen during deposition [21,42,43,53–58]. More recently, it was recognized that the detailed behavior of film roughening and morphology also depends sensitively on the existence of any counterbalancing downhill currents, $\underline{J}^{down}$. These could result from various features of the deposition dynamics near step edges, such as downward funneling and 'knockout' processes [16–20]. Molecular dynamics (MD) studies provide no evidence that 'knockout' or other transient processes contribute significantly to $\underline{J}^{down}$ for metal(100) homoepitaxy [16–20]. Thus, below we only consider downward funneling (see Fig. 6 for a schematic).

A more detailed picture of growth is based on consideration of the variation of these currents with local slope, $\underline{m}$. The currents are parallel to $\underline{m}$, and, by symmetry, vanish for $\underline{m}=\underline{0}$. The magnitude of $\underline{J}^{up}$ first increases with increasing $m=|\underline{m}|$, but then decreases for larger m due to narrow terraces inhibiting lateral mass flow. The magnitude of $\underline{J}^{down}$ should increase roughly linearly with increasing step-density, and thus with m. Also these currents are in opposite directions. Under conditions of mounding, the magnitude of the total current, $\underline{J}^{tot}=\underline{J}^{up}+\underline{J}^{down}$, will first increase from zero as m increases from zero, but then decrease through zero at some $m=m_0$, becoming negative for large m [55–57]. (A more detailed discussion of this behavior is given below.) Thus, from an initially flat surface, the slopes of mound facets tilted in the direction of $\underline{m}$ will grow until selecting the stable value m_0.

In the 2+1 dimensional systems of interest here, the square substrate symmetry tends to produce mounds with square pyramidal symmetry, with

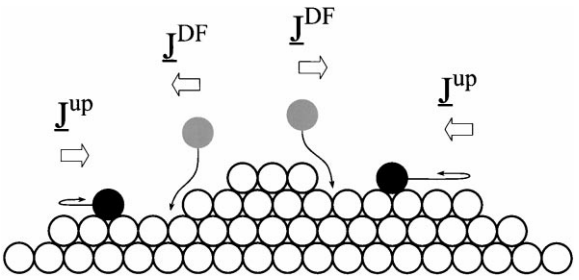

Fig. 6. Schematic of the uphill 'Schwoebel' current, J^{up}, and the downhill 'downward funneling' current, J^{DF}.

facets oriented in the [100] and [010] principal lattice directions [33–35,40,41,44–46]. Thus, not just the slope of mound facets, but also their orientation is selected. A simple mathematical form for the dependence of $\underline{J}^{tot}$ on $\underline{m}$ that produces selection of this specific orientation is given in Refs. [55–57], although the actual physical form must of course be more complicated. However, since we know a priori the selected [100] and [010] orientations of the mound facets, here, it is natural to consider just the dependence of the [100] component, J_x, of the currents on the [100] component, m_x, of the slope, thus determining the selected slope in this direction. The direction of increasing (decreasing) film height will be identified as right (left), for $m_x>0$ (<0). The discussion below is naturally cast in terms of the rescaled slope $M_x=am_x/b$, where 'a' is the horizontal lattice spacing, and 'b' is the vertical interlayer spacing, so $M_x=2m_x$ ($\sqrt{2}m_x$) for bcc (fcc) metals. For simplicity, both currents and distances will be specified in units where $a=1$.

We adopt the standard approach to quantify the lateral mass currents by simulation of deposition on vicinal surfaces with various global slopes, $\underline{m}(m_x,0)$, which are preserved during deposition. See Appendix B for a further discussion. Most studies determine only the variation of J_x^{tot} with $m_x\geq 0$. We find it instructive to separately determine and plot $J_x^{up}\geq 0$ and $|J_x^{down}|\geq 0$ versus $m_x\geq 0$, the crossing point of these curves determining the selected slope, m_{0x}. The data shown below are obtained after deposition of 20 ML for the case of small step-edge barrier with $\Gamma\approx 0.1$. Specifically, simulation parameters are chosen as $E_d=450$ meV, $E_{se}=30$ meV (so $\Gamma\approx 0.07$), $\nu=10^{11}\,s^{-1}$, and $F=0.7$ ML min^{-1}, reasonably describing Fe/Fe(100) homoepitaxy.

4.1. Uphill (destabilizing) current

For an infinite step-edge barrier, Johnson et al. [54] argue that the uphill Schwoebel current satisfies $J_x^{up}\sim F(\ell_c)^2 M_x$, for a small M_x. This corresponds to atoms deposited on terraces within a distance, ℓ_c, of an ascending step reaching that step, and those deposited further away nucleating into or aggregating with islands. Thus, ℓ_c measures the width of the zone adjacent to ascending steps denuded of islands. Since ℓ_c is known to scale like L_{av} [59], one can set $\ell_c=AL_{av}$, with A of order unity. For a larger M_x, corresponding to the step-flow regime, the form of the current crosses over to $J_x^{up}\sim F/M_x$. Assuming a simple interpolation between large and small M_x, they write [54]

$$J_x^{up}\propto FS(\ell_c)^2 M_x g(\ell_c M_x), \text{ with } g(z)=1/(1+z^2). \tag{3}$$

Here, the factor $S=1-\exp[-E_{se}/(k_BT)]$ rescales J_x^{up} to account for a finite step-edge barrier. This form of J_x^{up} assumes that behavior is controlled by a single characteristic length, ℓ_c. We emphasize that other choices of $g(z)$, satisfying $g(0)=1$ and $g(z)\sim 1/z^2$, for a large z, are equally plausible. A more sophisticated analysis, by Villain and coworkers [60,61], of the step-flow regime for larger M_x suggested a more complicated form for the uphill current,

$$J_x^{up}\propto F\ell_s\ell_c M_x/[(1+\ell_c M_x)(1+\ell_s M_x)], \tag{4}$$

involving a second characteristic 'Schwoebel length', $\ell_s\approx\exp[E_{se}/(k_BT)]-1$, which vanishes as S (or E_{se}) vanishes. However, Eq. (4) does not incorporate a sophisticated analysis of island nucleation, and thus of the small M_x regime.

In analyzing uphill current data for our model (Fig. 7), we find it most instructive to display the slope dependence of J_x^{up}/M_x, rather than of J_x^{up}. Such data are shown in Fig. 8 for the case of small step-edge barrier with $\Gamma\approx 0.1$. Simulation snapshots of the surface configurations for different T are shown in Fig. 9. One finds an initial decrease of J_x^{up}/M_x as M_x increases from zero, consistent with the form (4), or with a modified form (3) with, say, $g(z)=1/(1+z)^2$.

4.2. Downhill (stabilizing) current

For metal(100) homoepitaxy at lower T, the dominant contribution to the downhill current comes from the downward funneling process described in Section 1 [16–21], and we write $\underline{J}^{down}\approx\underline{J}^{DF}$. This process must be incorporated into the modeling [21–26,42,43] to consistently repro-

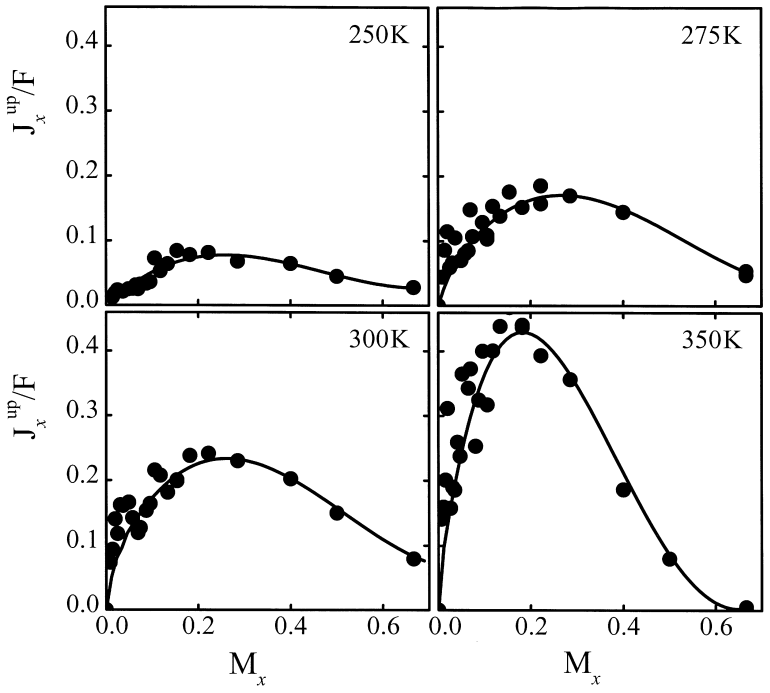

Fig. 7. Simulation results for the temperature dependence of J_x^{up}/F versus M_x. Parameters were chosen to roughly match Fe/Fe(100): $E_d = 450$ meV, $E_{se} = 30$ meV (so $\Gamma \approx 0.07$), $\nu = 10^{11}$ s^{-1}, and $F = 0.7$ ML min^{-1} [14,15,36–38].

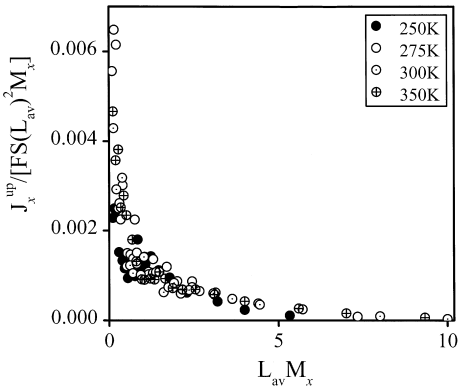

Fig. 8. Data in Fig.7 plotted as $J_x^{up}/[FS(L_{av})^2 M_x]$ versus $L_{av}M_x$ for $T = 250$, 275, 300, and 350 K, for which one has $L_{av} \approx 8$, 11, 14, and 20 (in units of 'a') and $S \approx 0.75$, 0.72, 0.69, and 0.63, respectively.

duce the observed roughening [36–38,40,41]. On a vicinal surface, one expects that the magnitude of the downhill 'downward funneling' current, J_x^{DF}, is primarily controlled by the net step-density, i.e. the difference between densities of ascending and descending steps (weighted by step height). Since this net step-density should scale like the global surface slope, one expects that

$$J_x^{DF} \approx -FC_{DF}M_x, \tag{5}$$

as recognized in early studies of funneling [16–20]. Our simulation results confirm a near-linear dependence of J_x^{DF} on M_x. However, we should emphasize that the coefficient of proportionality, C_{DF}, is non-trivial, as it is determined by the 'locally equilibrated' film morphology, rather than by that of a perfect vicinal surface. Since the precise value of C_{DF} affects slope selection, we present a detailed analysis below.

To this end, it is instructive to first determine the relationship between J_x^{DF} and M_x for perfect vicinal surfaces (ascending from left to right for $M_x > 0$). Detailed analysis of our model in Appendix C shows that $C_{DF} = 3/8$ for a perfect 'staircase' of single steps, and $C_{DF} = (2+k)/8$ for height $-k$ steps. This suggests that for a sufficiently high T, where the surface has predominantly single

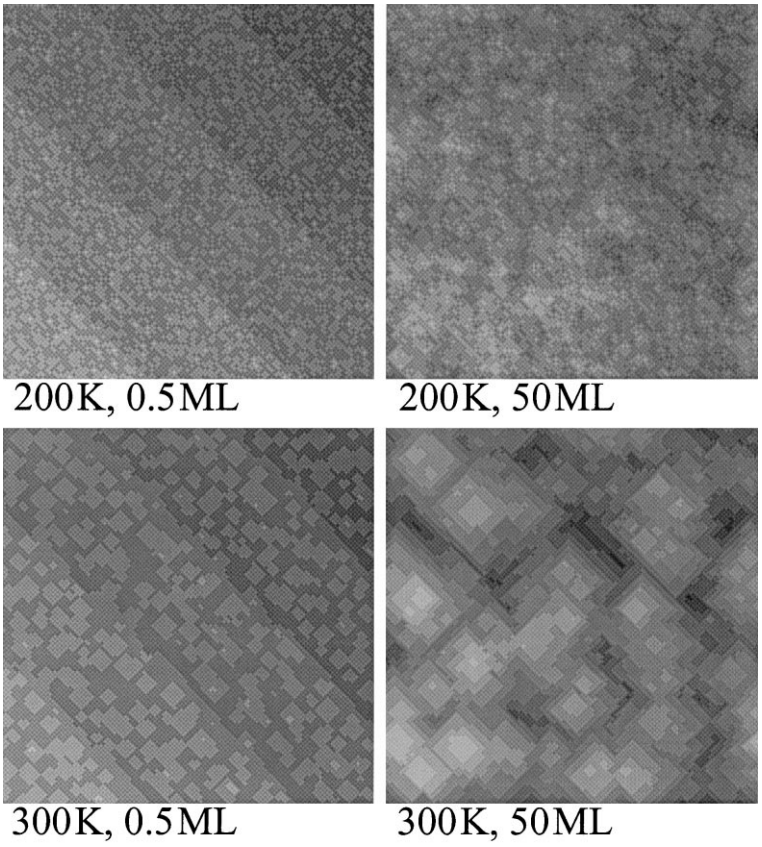

Fig. 9. Snapshots of a $170a/\sqrt{2} \times 170a/\sqrt{2}$ region of 0.5 and 50 ML films obtained in simulations at 200 K ($h/F \approx 10^2$) and 300 K ($h/F \approx 10^6$), as indicated, for a perfect vicinal surface, using parameters as in Fig.7. Darker regions have lower height.

steps, one should find that $C_{DF} \approx 3/8$, and also that C_{DF} should increase for a lower T where a greater number of multiple steps likely occur due to higher local slopes. Indeed, the simulation data for our model shown in Fig. 10 for a small step-edge barrier with $\Gamma \approx 0.1$ are entirely consistent with this proposed trend.

Of course, a picture of the growing surface as a staircase of equal height steps is overly simplistic. Consider the evolution of a surface during deposition from an initial perfect staircase of single-steps, with a small $M_x > 0$. Initially, isolated islands are formed on the broad terraces, but this has little effect on J_x^{DF} since there are equal contributions to the current to the left and right from funneling off left and right island edges, respectively. As growth continues, islands merge with ascending steps, which effectively replaces straight

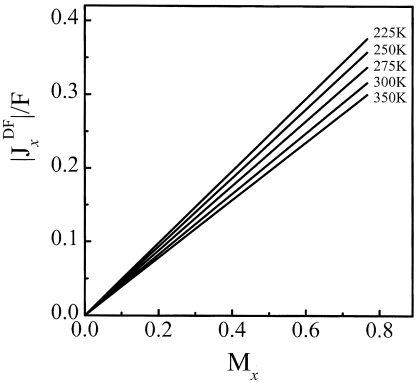

Fig. 10. Simulation results for the temperature dependence of $|J_x^{DF}|/F$ versus M_x, using parameters as in Fig.7. The slopes give $C_{DF} \approx 0.491$, 0.467, 0.440, 0.413, and 0.392, at $T = 225$, 250, 275, 300, and 350 K, respectively.

steps with meandering steps (cf. Fig. 9), and should not significantly affect J_x^{DF}. However, any islands reaching descending steps effectively replace a single-step-up configuration with a paired double-step-up and single-step-down configuration, which increases $|J_x^{DF}|$ (see Appendix C).

5. Mounding, slope selection, and the kinetic phase transition

For the formation of mounds, the uphill current must be sufficiently strong that $J_x^{tot} = J_x^{up} + J_x^{down} > 0$ for a small M_x. Let $J_x^{DF} = -FC_{DF}M_x$, and assume that $J_x^{up} \approx AFS(L_{av})^2 M_x$ for small M_x, with A of order unity. Then one requires that $\partial J_x^{up}/\partial M_x \approx AFS(L_{av})^2$ exceeds $|\partial J_x^{DF}/\partial M_x| \approx FC_{DF}$, as is expected for a moderate and higher T (where L_{av} is large). Then, as noted in Section 4, the mound facets oriented in the [100] direction select a slope, M_{0x}, which satisfies the condition $J_x^{up} = |J_x^{DF}|$. For a large selected slope corresponding to the step-flow regime ($\ell_c M_x \gg 1$), the expression (4) of Villain et al. [60,61] for $J_x^{up} \approx BF_s/(1+\ell_s M_x)$, with B of order unity, implies that $M_{0x} \approx [(1/\ell_s^2 + 4B/C_{DF})^{1/2} - 1/\ell_s]/2$, which is expected to increase with decreasing T (corresponding to increasing ℓ_s). The same trend is found using $J_x^{up} \propto FS/M_x$ from Eq. (3), or other modified expressions for J_x^{up} [62]. However, corrections to J_x^{up} for smaller slopes could produce the opposite trend. Thus, for a precise and general analysis of the behavior of M_{0x}, it is appropriate to utilize the simulation results for the currents from Section 4.

In Fig. 11, we show simulation results for the behavior of J_x^{up} and $|J_x^{DF}|$ versus M_x, for a small step-edge barrier with $\Gamma \approx 0.1$ and for a broad range of T. For a higher T, the scenario indicated above for mound formation and slope selection applies. However, the selected slope, M_{0x}, varies only weakly (decreasing slightly) over a broad range of T. As the temperature decreases further and thermal diffusion is strongly inhibited, one finds that J_x^{up} is reduced significantly, and the value of $\partial J_x^{up}/\partial M_x$ at $M_x = 0$ decreases below $|\partial J_x^{DF}/\partial M_x| \approx FC_{DF}$. At this point, the uphill Schwoebel current becomes too small to counterbalance the downhill downward funneling current, and there is a kinetic phase transition from 'mounding' to 'smooth growth' with $\beta \approx 0$. The selected slope, M_{0x}, also decreases to zero as T decreases toward this transition.

The observed variation of M_{0x} with T does not correspond to the previously described behavior of the 'local slope' obtained from the local step-density. The latter increases monotonically with decreasing T and is non-zero for smooth growth (below the transition) with $\beta \approx 0$. This difference should be expected since the selected 'global' slope of the sides of large mounds is determined from the net step-density, in contrast to the 'local slope' that is determined from the total step-density. However, it is plausible that the 'local slope' and the selected slopes would be similar in magnitude for T well above the transition. This is found in our simulations mimicking Fe/Fe(100) growth at 300 K, both slope estimates agreeing with experimental observations. A similar consistency is expected for Ag/Ag(100), where experimental data for the selected slope are not available. We have already noted that our model does not describe behavior for multilayer Cu/Cu(100). Finally, we note that the selected slope, M_{0x}, from simulation results for the currents corresponds to that for very large coarsened mounds, and thus only to experimental behavior for sufficiently thick films (cf. Ref. [52]).

6. 'Anomalous' behavior for low temperature

6.1. Long-range lateral correlations at low T

For low T, where terrace diffusion is inoperative, one does not expect significant island formation, so submonolayer lateral spatial correlations in the adlayer should be of a short range. However, high-resolution diffraction studies have revealed that large lateral correlation lengths of $\sim 10a$ persist to temperatures as low as 80 K [63,64]! One possible source of such a correlation derives from the very low activation barriers that exist for both thermal diffusion along close packed step edges, and for diagonally adjacent adatoms to move into a neighboring configuration [25,26,65]. Together, these could allow significant restructuring or 'clumping'

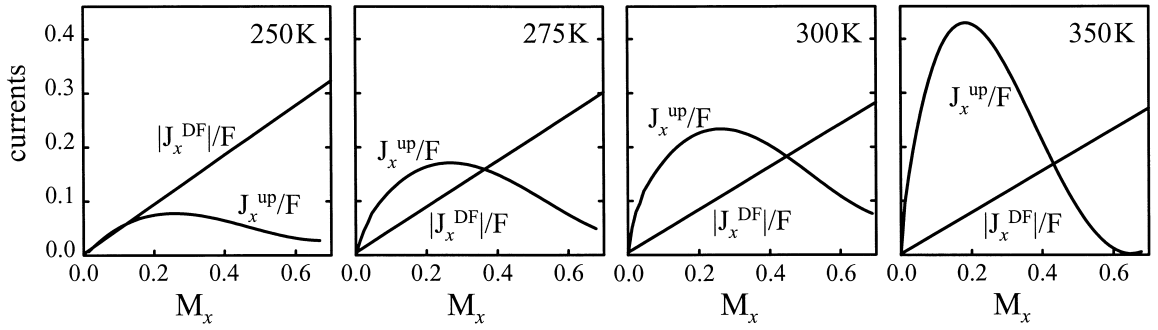

Fig. 11. Temperature dependence of the variation of the uphill and downhill currents with slope (data from Figs. 7 and 9). This sequence illustrates the kinetic phase transition as T decreases and the curves for the two currents 'uncross'.

of the adlayer deposited at a low T where most atoms land near to other adatoms (M. Breeman, pers. commun.; see also [66]). Another possible source of 'clumping' at low T in metal(100) homoepitaxial systems derives from the feature that deposited atoms have a significant excess kinetic energy upon impact. Whereas one does not find a significant 'transient mobility' of isolated deposited atoms [16–20], there may be some 'transient clumping' of atoms deposited near to other adatoms [25,26,67]. Finally, we note that these low T clumping processes would likely provide an additional contribution to the uphill current, not included in our modeling. This would modify slope selection at a lower T and the kinetic phase transition.

6.2. Breakdown of downward funneling

In the initial MD studies demonstrating the existence of the downward funneling process in metal(100) homoepitaxy [16–20] and in subsequent more detailed analyses [68], it was noted that depositing atoms can be caught at threefold hollow (3FH) sites on the sides of sufficiently large {111} microfacets, rather than funneling to the bottom. Such microstructures might be more prevalent at lower T where there are larger 'local slopes'. However, for metal(100) homoepitaxial growth, we expect a further important effect at least partly compensating for this breakdown. In the lower T regime around 100 K, diffusion of isolated atoms on {100} terraces is typically negligible, but diffusion on {111} microfacets may well still be quite rapid due to a much lower activation barrier. Thus, although atoms deposited on such microfacets may be thermally accommodated before reaching 4FH sites at the bottom, one might expect that they will quickly diffuse randomly around the microfacets until they become trapped at the 4FH sites at the bottom which provide 'sinks' for the diffusing adatoms [22]. This type of thermal motion might be viewed as constituting a downhill Schwoebel current that would effectively recover the same growth behavior as for 'perfect' downward funneling [22].

However, the steep local microprotrusions, typically present in low T growth, present a variety of complicated local geometries. Some of these will likely trap deposited adatoms at epitaxial non-4FH sites more effectively than do the 3FH sites on the sides of simple {111} microfacets. We can categorize such 'trap sites' according to the number (p) of supporting atoms in the layer beneath, and the number (q) of in-layer nearest-neighbor atoms, and denote these as S_p^q sites. Thus, 4FH adsorption sites are S_4^q sites, and 3FH sites on {111} microfacets are S_2^1 (and S_1^2) sites. [S_2^1 sites are not epitaxial with respect to the growing fcc or bcc crystal.] We expect that the S_3^q sites could play a particularly important role as 'traps', and such sites should have (statistically) significant populations at least for $q=0$ and $q=1$. Although the S_3^0 sites may not trap that effectively, certainly S_3^1 sites will be much more likely to trap than 3FH S_2^1 sites (see Fig. 12). The barrier to escape from S_3^1 sites will no doubt be higher than the diffusion barrier on {111} facets, so adatoms trapped at such sites will have

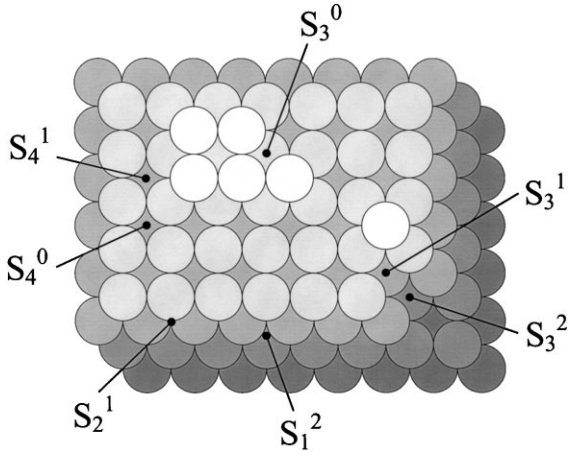

Fig. 12. Schematic of key trap sites, S_1^2, S_2^1, S_3^0, S_3^1 and S_3^2, that induce a breakdown of downward funneling deposition dynamics, and enhance overhang and defect formation.

more difficulty in reaching lower 4FH sites. Trapping at these sites can thus significantly influence the film growth mode and morphology, as discussed below.

6.3. Multilayer growth at $T \approx 0$ K

At $T \approx 0$ K, an atom that is accommodated at a non-4FH site will not be able to escape via any thermal diffusion process (although the possibility of 'knockdown' by subsequently deposited atoms exists). Thus, one should expect a breakdown of the predictions of growth models incorporating simple downward funneling. It is clear that once non-4FH epitaxial sites can be populated, the possibility exists for the formation of overhangs, and even enclosed voids or defects. Indeed, the spontaneous creation of voids has been observed in recent MD studies of low-T metal(100) homoepitaxy [27,28]. No doubt, a detailed analysis of the mechanistic genesis of their formation would reveal the key role of trapping at S_3^q sites. The other key observation of these MD studies was rough film growth. Certainly, precise characterization or prediction of roughening would depend on the details of the breakdown of funneling, and of the formation of overhangs and voids. However, some generic insight into the roughening of films incorporating bulk defects is available. It is well known that in simplistic 'epitaxial growth' models with bulk defects, such as 'ballistic deposition' [69] and 'random sequential adsorption' [70,71], roughening is described by non-linear Kardar–Parisi–Zhang (KPZ) evolution. Here, one has $W \sim \theta^{1/4}$ (in $2+1$ dimensions), if enclosed voids are ignored in the determination of W [32]. The origin of the KPZ non-linearity is simply that for deposition on a vicinal substrate, the volume density of bulk defects formed depends on the substrate tilt. Since this is expected to be a feature of more realistic models (cf. Ref. [72]), it is reasonable to expect KPZ-type roughening for low T deposition in metal(100) homoepitaxy.

7. Conclusions

We have provided a comprehensive analysis of the temperature (T) dependence of roughening for a realistic model of metal(100) homoepitaxy. In particular, we identified a kinetic phase transition from a regime of 'mounding' at higher T, to one of reentrant 'smooth growth' at lower T. All quantities of interest vary strongly with T in the mounding regime, including the effective exponent for roughening. Thus, the concept of universal (asymptotic) exponents [32] has limited practical applicability in the regime of interest for these experiments.

In closing, we comment briefly on other related work, and on natural extensions to this study. Recently, it was observed that the presence of long-range attractions between diffusing adatoms and step-edges induces a destabilizing uphill current. This leads to mounding, even in the absence of an Ehrlich–Schwoebel barrier [73]. It is not yet clear whether this effect is significant in metal(100) homoepitaxy. Another study proposed a transition from 'mounding' to smooth growth as T increases above some 'high' critical value (which is distinct from the low-T transition discussed above) [62]. However, the underlying analysis utilized an expression for $\underline{J}^{up}$ based on perfect vicinal surfaces in the step-flow regime, so its accuracy is unclear near a transition where the selected slope vanishes and island nucleation becomes significant. Future studies should systematically explore the influence

of reversibility in submonolayer island formation on subsequent multilayer growth. Reversibility results in enhanced depletion of nearby 2D island pairs in the submonolayer regime [29,74]. This leads to greater 'ordering' of 2D islands, and thus of the multilayer mounds, as well as enhanced splitting of diffraction profiles [21]. Finally, for a reliable analysis of the unusual features of growth at low T, it would be appropriate to introduce refined system-specific models accounting for both intralayer 'clumping' of nearby adatoms, and trapping of deposited atoms at non-4FH sites.

Acknowledgements

This work was supported by NSF Grant No. CHE-9700592, and performed at Ames Laboratory (J.W.E.). Ames Laboratory is operated for the US DOE by Iowa State University under Contract No. W-7405-Eng-82. It was also supported by the Office of Basic Energy Sciences, Division of Materials Sciences, of the US DOE, and performed at Sandia National Laboratories (M.C.B.). Sandia is a multiprogram laboratory operated for the US DOE by Sandia Corporation, a Lockheed Martin Company, under Contract No. DE-AC04-94AL85000.

Appendix A: Discrete treatment of deposition dynamics

A bird's-eye view of the surface of a growing film for fcc or bcc metal(100) homoepitaxy reveals two interpenetrating subarrays of vertical columns of atoms, labeled '+' and '−' in Fig. 13. Atoms at the top of one set of columns are in even layers, and those in the other are in odd layers. For growth with no overhangs or internal vacancies, the top atoms in adjacent columns of different subarrays have a height difference of unity. This geometry is equivalent to that of the so-called single-step model for film growth [75]. As in previous studies [16–26], we naturally replace deposition with continuous lateral coordinates with deposition on top of 'discrete' columns chosen randomly in either of the two subarrays. If the vacant epitaxial site on top of the chosen column is a 4FH site (i.e. the top occupied site in all four adjacent columns is one level lower), then the deposited atom remains there. Otherwise, it randomly funnels down to lower layers until a 4FH site is found [16–20].

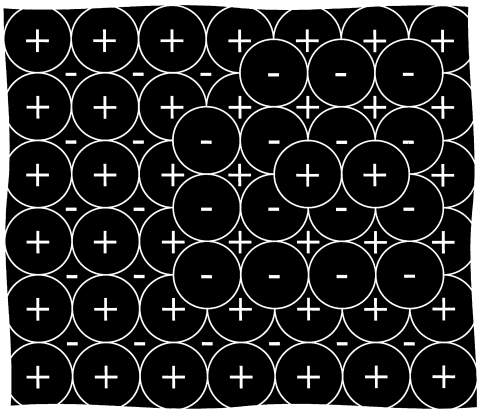

Fig. 13. Bird's-eye view of the geometry of a growing surface during metal(100) homoepitaxy. Subarrays of vertical columns are indicated by + and −.

Appendix B: Simulation of slope dependence of mass currents

For elucidation of the morphology of growing films, the behavior of the lateral mass currents of deposited atoms for a 'locally equilibrated' growing surface is relevant (rather than behavior for a perfect vicinal surface) (see Fig. 9). Thus, whereas currents determined after incremental deposition on a perfect vicinal surface display a qualitatively reasonable $\underline{m}$-dependence [42,43,54], more prolonged deposition is appropriate. For larger slopes, $m_x \geq m_{0x}$, equilibration is presumably rapid, and we emphasize that behavior in this regime is actually sufficient to determine m_{0x}! However, for slopes $m_x < m_{0x}$, an infinite growing surface will facet into regions of selected slope, $\pm m_{0x}$, and so, strictly, J's should be measured for a judicious choice of finite deposition time or finite system size ($\gg L_{av}$). In the simulations, we used perfect vicinal surfaces of single-steps where 20 ML were

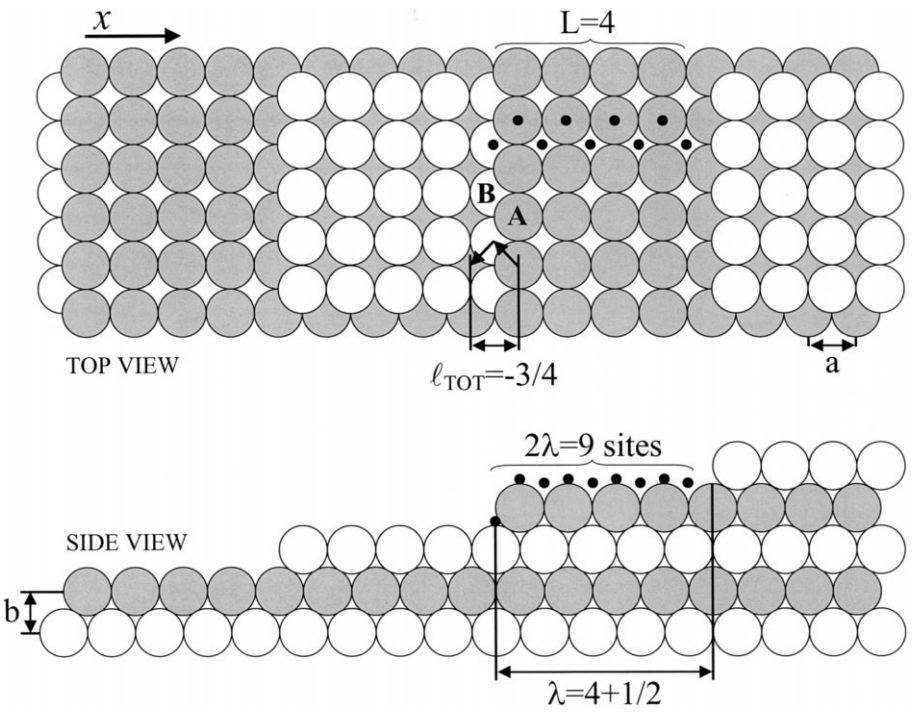

Fig. 14. Top and side views of a periodic vicinal staircase of single-steps (up from left to right). Here, $k=1$, $L=4$, and $\lambda=9/2$, and $p_A=1/2$, $d_A=-1/2$, $p_B=1$, $d_B=-1/2$.

deposited. The currents were then monitored for an additional 0.2 ML.

Appendix C: Analysis of the downward funneling current

We consider atoms depositing on two classes of periodic vicinal surfaces, oriented in the [100] direction. We determine the mean lateral displacement of deposited atoms, $\langle \ell_{DF} \rangle$, and thus the lateral flux, $J_x^{DF}=F\langle \ell_{DF} \rangle$, due to the downward funneling deposition dynamics. Furthermore, we note the consistency between continuum and discrete treatments of deposition [16–20]. In the former, atoms impinge on the surface with continuous lateral positions chosen randomly well above the surface. One determines the lateral displacement for each position, and obtains a mean displacement after integrating over one period of the vicinal surface (and then normalizing). In the latter, atoms deposit randomly at discrete locations on top of the two subarrays of vertical columns of atoms composing the film. Now, one determines the lateral displacement for each discrete position, and obtains a mean after summing over one period. Specifically, we let p_i denote the probability of funneling down for an atom deposited on top of site i, and d_i the extra lateral displacement to the lower 4FH site on funneling down, compared with the hopping in-plane (d_i is measured in units of 'a', and is negative if along $-x$.) Then, the total lateral displacement of atoms deposited within a period (λa) is $\ell_{TOT}=\sum_i p_i d_i$, and the mean lateral displacement is $\langle \ell_{DF} \rangle = \ell_{TOT}/(2\lambda)$.

Class 1: A perfect staircase with steps of height k atoms and terraces with L fully exposed atoms, ascending from left to right (see Fig. 14). Here, the lateral periodicity is $\lambda=L+k/2$, in units of 'a', and the global slope is $M_x=k/\lambda$. In this case, one finds a mean lateral displacement to the left of $\langle \ell_{DF} \rangle = k(k+2)/(8\lambda)$, in units of 'a', so $|J_x^{DF}| = F(k+2)M_x/8$, and $C_{DF}=(k+2)/8$, as stated in the text. We note that our result $C_{DF}=3/8$ for

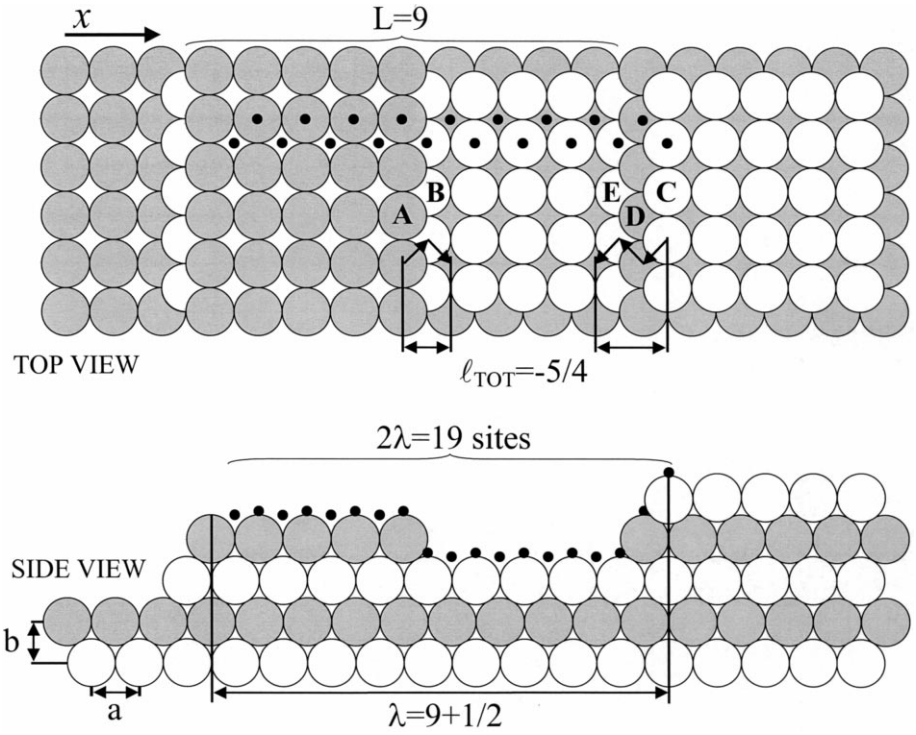

Fig. 15. Top and side views of a periodic vicinal staircase of pairs of double-step up and single-step down, from left to right. Here, $k=1$, $L=9$, and $\lambda=19/2$, and $p_A=1/2$, $d_A=+1/2$, $p_B=1$, $d_B=+1/2$, $p_C=1/2$, $d_C=-1$, $p_D=1$, $d_D=-1$, $p_E=1$, $d_E=-1/2$.

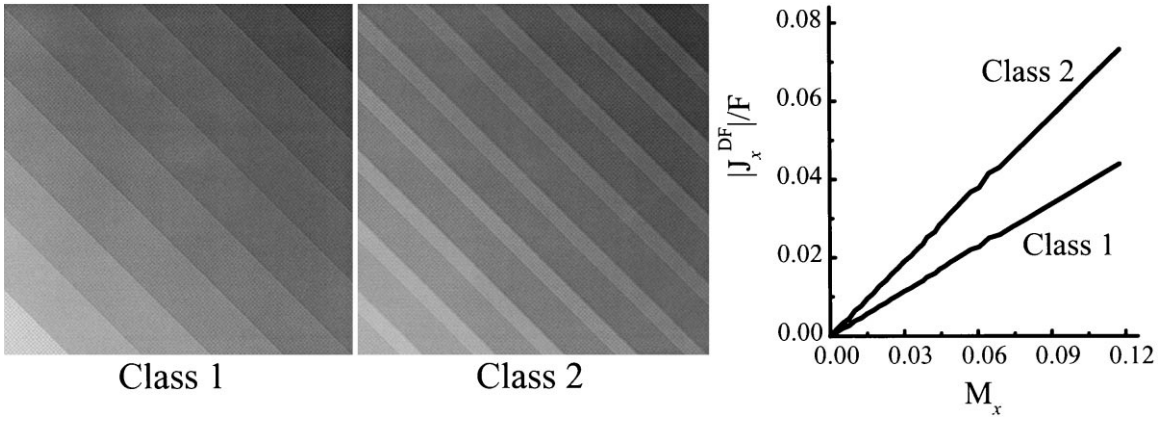

Fig. 16. Snapshots of $170a/\sqrt{2}\times 170a/\sqrt{2}$ regions of periodic vicinal staircases with (a) single-steps up, and (b) pairs of double-step up and single-step down. Darker regions have a lower height. (c) Corresponding simulation results for $|J_x^{DF}|/F$ versus M_x. The slopes give $C_{DF}\approx 0.377$ (Class 1) and $C_{DF}\approx 0.629$ (Class 2).

$k=1$ (Fig. 14) appears inconsistent with a calculation in Refs. [42,43], but this is only because part of J_x^{DF} was assigned to (i.e. subtracted from) J_x^{up} in that analysis.

Class 2: A staircase composed of pairs of steps of height $k+1$ atoms up, and height 1 atom down, and lateral periodicity $\lambda=L+k/2$ (see Fig. 15). Here, the global slope is $M_x=k/\lambda$, as in

Class 1, but now one finds a mean lateral displacement to the left of $\langle \ell_{DF} \rangle = k(k+4)/(8\lambda)$, so $|J_x^{DF}| = F(k+4)M_x/8$, and $C_{DF} = (k+4)/8$. Thus, one has $C_{DF} = 5/8$ for a paired double-step up and single-step down staircase (Fig.15), versus $C_{DF} = 3/8$ for a perfect single-step vicinal staircase (Fig. 14) with the same slope. Simulations duplicate these exact results (see Fig. 16).

References

[1] M.G. Lagally (Ed.), Kinetics of Ordering and Growth at Surfaces, Plenum, New York, 1990.
[2] J.D. Weeks, G.H. Gilmer, Adv. Chem. Phys. 40 (1979) 157.
[3] F. Reif, Fundamentals in Statistical and Thermal Physics, McGraw-Hill, New York, 1965, p. 42.
[4] R. Kunkel, B. Poelsema, L.K. Verheij, G. Comsa, Phys. Rev. Lett. 65 (1990) 733.
[5] M. Bott, T. Michely, G. Comsa, Surf. Sci. 272 (1992) 161.
[6] H.A. van der Vegt, H.M. van Pinxteren, M. Lohmeier, E. Vlieg, J.M.C. Thornton, Phys. Rev. Lett. 68 (1992) 3335.
[7] M. Henzler, T. Schmidt, E.Z. Lu, in: S.Y. Xie, Tong, M.A. Van Hove (Eds.), World Scientific, Singapore, 1994..
[8] W. Wulfhekel, N.N. Lipkin, J. Kliewer, G. Rosenfeld, L.C. Jorritsma, B. Poelsema, G. Comsa, Surf. Sci. 384 (1998) 227.
[9] G. Ehrlich, F.G. Hudda, J. Chem. Phys. 44 (1966) 1039.
[10] R.L. Schwoebel, E.J. Shipsey, J. Appl. Phys. 37 (1966) 3682.
[11] J. Jacobsen, K.W. Jacobsen, P. Stoltze, J.K. Nørskov, Phys. Rev. Lett. 74 (1995) 2295.
[12] J.W. Evans, M.C. Bartelt, in: Z. Zhang, M.G. Lagally (Eds.), Morphological Organization in Epitaxial Growth and Removal, World Scientific, Singapore, 1998.
[13] W.F. Egelhoff, I. Jacob, Phys. Rev. Lett. 62 (1989) 921.
[14] D.K. Flynn-Sanders, J.W. Evans, P.A. Thiel, Surf. Sci. 289 (1993) 77.
[15] D.K. Flynn-Sanders, J.W. Evans, P.A. Thiel, J. Vac. Sci. Technol. A 7 (1989) 2162.
[16] J.W. Evans, D.E. Sanders, P.A. Thiel, A.E. DePristo, Phys. Rev. B 41 (1990) 5410.
[17] J.W. Evans, Vacuum 41 (1990) 479.
[18] J.W. Evans, Phys. Rev. B 43 (1991) 3897.
[19] D.E. Sanders, J.W. Evans, in: S.Y. Tong, M.A. Van Hove, K. Takayanagi, X.D. Xie (Eds.), Springer, Berlin, 1991.
[20] H.C. Kang, J.W. Evans, Surf. Sci. 271 (1992) 321.
[21] M.C. Bartelt, J.W. Evans, Phys. Rev. Lett. 75 (1995) 4250.
[22] M.C. Bartelt, J.W. Evans, MRS Proc. 399 (1996) 89.
[23] M.C. Bartelt, J.W. Evans, Bull. Am. Phys. Soc. 41 (1996) 389.
[24] M.C. Bartelt, J.W. Evans, Bull. Am. Phys. Soc. 42 (1997) 575.
[25] J.W. Evans, M.C. Bartelt, Langmuir 12 (1996) 217.
[26] J.W. Evans, M.C. Bartelt, in: M.C. Tringides (Ed.), Surface Diffusion: Atomistic and Collective Processes, Proc. NATO ASI, Series B: Physics Vol. 360 , Plenum, New York, 1997, p. 197.
[27] C.L. Kelchner, A.E. DePristo, J. Vac. Sci. Technol. A 14 (1996) 1633.
[28] C.L. Kelchner, A.E. DePristo, Surf. Sci. 393 (1997) 72.
[29] J.A. Venables, Phil. Mag. 27 (1973) 697.
[30] M.C. Bartelt, J.W. Evans, Surf. Sci. 298 (1993) 421.
[31] M.C. Bartelt, J.W. Evans, MRS Proc. 312 (1993) 255.
[32] A.-L. Barabási, H.E. Stanley, Fractal Concepts in Surface Growth, Cambridge University Press, Cambridge, 1995.
[33] C.-M. Zhang, M.C. Bartelt, J.-M. Wen, C.J. Jenks, J.W. Evans, P.A. Thiel, Surf. Sci. 406 (1998) 178.
[34] C.-M. Zhang, M.C. Bartelt, J.-M. Wen, C.J. Jenks, J.W. Evans, P.A. Thiel, J. Crystal Growth 174 (1997) 851.
[35] L. Bardotti, C.R. Stoldt, C.J. Jenks, M.C. Bartelt, J.W. Evans, P.A. Thiel, Phys. Rev. B 57 (1998) 12544.
[36] W.C. Elliott, P.F. Miceli, T. Tse, P.W. Stephens, Physica B 221 (1996) 65.
[37] W.C. Elliott, P.F. Miceli, T. Tse, P.W. Stephens, Phys. Rev. B 54 (1996) 17938.
[38] W.C. Elliot, P.F. Micelli, T. Tse, P.W. Stephens, in: M.C. Tringides (Ed.), Surface Diffusion: Atomistic and Collective Processes, Proc. NATO ASI, Series B: Physics Vol. 360, Plenum, New York, 1997, p. 209.
[39] J. Alvarez, E. Lundgren, X. Torrelles, S. Ferrer, Phys. Rev. B 57 (1998) 6325.
[40] J.A. Stroscio, D.T. Pierce, R.A. Dragoset, Phys. Rev. Lett. 70 (1993) 3615.
[41] J.A. Stroscio, D.T. Pierce, M. Stiles, A. Zangwill, L.M. Sander, Phys. Rev. Lett. 75 (1995) 4246.
[42] J.G. Amar, F. Family, Phys. Rev. B 54 (1996) 14742.
[43] J.G. Amar, F. Family, Phys. Rev. B 52 (1995) 13801.
[44] H.J. Ernst, F. Fabre, R. Folkerts, J. Lapujoulade, Phys. Rev. Lett. 72 (1994) 112.
[45] H.J. Ernst, F. Fabre, R. Folkerts, J. Lapujoulade, J. Vac. Sci. Technol. A 12 (1994) 1809.
[46] L.C. Jorritsma, M. Bijnagte, G. Rosenfeld, B. Poelsema, Phys. Rev. Lett. 78 (1997) 911.
[47] H. Dürr, J.F. Wendelken, J.K. Zuo, Surf. Sci. 328 (1995) L527.
[48] W.W. Pai, A.K. Swan, Z. Zhang, J.F. Wendelken, Phys. Rev. Lett. 79 (1997) 3210.
[49] J.-M. Wen, J.W. Evans, M.C. Bartelt, J.W. Burnett, P.A. Thiel, Phys. Rev. Lett. 76 (1996) 652.
[50] C.R. Stoldt, A.M. Cadilhe, C.J. Jenks, J.-M. Wen, J.W. Evans, P.A. Thiel, Phys. Rev. Lett. 81 (1998) 2950.
[51] H.J. Ernst, Surf. Sci. 383 (1997) L755.
[52] J.-K. Zuo, J.F. Wendelken, Phys. Rev. Lett. 78 (1997) 2791.
[53] J. Villain, J. Physique I 1 (1991) 19.
[54] M.D. Johnson, C. Orme, A.W. Hunt, D. Graff, J. Sudijono, L.M. Sander, B.G. Orr, Phys. Rev. Lett. 72 (1994) 116.
[55] M. Siegert, M. Plischke, Phys. Rev. Lett. 73 (1994) 1517.

[56] M. Siegert, M. Plischke, Phys. Rev. E 53 (1996) 307.
[57] J. Krug, M. Plischke, M. Siegert, Phys. Rev. Lett. 70 (1993) 3271.
[58] P. Smilauer, D.D. Vvedensky, Phys. Rev. B 52 (1995) 14263.
[59] Y.-W. Mo, J. Kleiner, M.B. Webb, M.G. Lagally, Surf. Sci. 268 (1992) 275.
[60] P. Politi, J. Villain, Phys. Rev. B 54 (1996) 5114.
[61] I. Elkinani, J. Villain, J. Physique I (France) 4 (1994) 949.
[62] J.G. Amar, F. Family, Phys. Rev. B 54 (1996) 14071.
[63] H.J. Ernst, F. Fabre, J. Lapujoulade, Phys. Rev. B 46 (1992) 1929.
[64] G.I. Nyberg, M.T. Kief, W.F. Egelhoff, Phys. Rev. B 48 (1993) 14509.
[65] A.F. Voter, SPIE 821 (1987) 214.
[66] M. Breeman , G.T. Barkema , M.H. Langelaar , D.O. Boerma , Thin Solid Films 272 (1996) 195.
[67] G. Vandoni, C. Felix, R. Monot, J. Buttet, W. Harbich, Surf. Sci. 320 (1994) L63.
[68] D.M. Halstead, A.E. DePristo, Surf. Sci. 286 (1993) 275.
[69] Y.P. Pellegrini, R. Jullien, Phys. Rev. Lett. 64 (1990) 1745.
[70] J.W. Evans, Rev. Mod. Phys. 65 (1993) 1281.
[71] P. Nielaba, V. Privman, Phys. Rev. E 51 (1995) 2022.
[72] M. Schimschak, J. Krug, Phys. Rev. B 52 (1995) 8550.
[73] J.G. Amar, F. Family, Phys. Rev. Lett. 77 (1996) 4584.
[74] J.W. Evans, M.C. Bartelt, J. Vac. Sci. Technol. A 12 (1994) 1800.
[75] P. Meakin, R. Ramanlal, L.M. Sander, R.C. Ball, Phys. Rev. A 34 (1986) 5091.